Acta Materialia 282 (2025) 120455

Contents lists available at ScienceDirect

Acta Materialia

journal homepage: www.elsevier.com/locate/actamat

Full length article

Enabling quantitative analysis of *in situ* TEM experiments: A high-throughput, deep learning-based approach tailored to the dynamics of dislocations

Hengxu Song [a,1], Binh Duong Nguyen [a], Kishan Govind [a], Dénes Berta [b], Péter Dusán Ispánovity [a,b], Marc Legros [c], Stefan Sandfeld [a,d,*]

[a] Institute for Advanced Simulations – Materials Data Science and Informatics (IAS-9), Forschungszentrum Jülich GmbH, Jülich, 52425, Germany
[b] Department of Materials Physics, ELTE Eötvös Loránd University, Pázmány P. stny. 1/A, Budapest, 1117, Hungary
[c] CEMES-CNRS, Toulouse, 31055, France
[d] Chair of Materials Data Science and Materials Informatics, Faculty 5 – Georesources and Materials Engineering, RWTH Aachen University, Aachen, 52056, Germany

ARTICLE INFO

Dataset link: https://zenodo.org/doi/10.5281/zenodo.10800695

Keywords:
Dislocation avalanche
Deep learning
High-entropy alloy
In situ TEM

ABSTRACT

In situ TEM is by far the most commonly used microscopy method for imaging dislocations, i.e., line-like defects in crystalline materials. However, quantitative image analysis so far was not possible, implying that also statistical analyses were strongly limited. In this work, we created a deep learning-based digital twin of an *in situ* TEM straining experiment, additionally allowing to perform matching simulations. As application we extract spatio-temporal information of moving dislocations from experiments carried out on a Cantor high entropy alloy and investigate the universality class of plastic strain avalanches. We can directly observe "stick–slip motion" of single dislocations and compute the corresponding avalanche statistics. The distributions turn out to be scale-free, and the exponent of the power law distribution exhibits independence on the driving stress. The introduced methodology is entirely generic and has the potential to turn meso-scale TEM microscopy into a truly quantitative and reproducible approach.

1. Introduction

Metals and alloys are by far the most important structural materials due to their high yield strength combined with great ductility allowing materials to undergo significant deformations without failure. One of the "key ingredients" for improving mechanical properties are, quite unintuitively, defects in the crystalline structure, such as line-like dislocations. In particular in alloys, they exhibit complex behavior that is up to date not fully understood.

The development of alloys with optimal strength-ductility properties was strongly accelerated by the discovery of high entropy alloys (HEAs): multi-principal-element alloys containing at least five components [1,2]. Their high configurational entropy leads to a random or near-random order of the alloying atoms [3]. Apart from, e.g., enhanced corrosion resistance and thermal stability [4] this also results in exceptional mechanical properties [5–8]. Exploring the interaction of dislocations with such aspects of randomness and connecting this to emergent properties is challenging because it is exactly the randomness that requires large datasets for separating "the noise from the signal" during statistical analyses. This is a particular challenge in the context of experiments and even more so in the context of *in situ* microscopy.

The alloying atoms in HEAs occupy random lattice sites on a typically face- or body-centered cubic (FCC or BCC) crystal lattice such as the FCC CoCrFeMnNi alloy, the so-called "Cantor-alloy" [9]. Since the alloying elements have different atomic radii, the crystal lattice is strongly distorted, resulting in appreciable random fluctuations of the local elastic distortions and stresses [10,11]. Such distorted sites interact with dislocations and may act as pinning centers that hinder the motion of gliding dislocations and, thereby, increase the yield strength of HEAs significantly. However, accurate and quantitative estimation of how this affects hardening is still difficult.

Investigating hardening and the yield stress of HEAs was successfully done by assuming a sinusoidal dislocation shape that minimizes

* Corresponding author at: Institute for Advanced Simulations – Materials Data Science and Informatics (IAS-9), Forschungszentrum Jülich GmbH, Jülich, 52425, Germany.
E-mail address: s.sandfeld@fz-juelich.de (S. Sandfeld).

[1] Current affiliation of H. Song: LNM, Institute of Mechanics, Chinese Academy of Sciences, Beijing 100190, China, as well as: School of Engineering Science, UCAS, Beijing 100049, China.

https://doi.org/10.1016/j.actamat.2024.120455
Received 22 July 2024; Received in revised form 4 October 2024; Accepted 4 October 2024
Available online 28 October 2024

the sum of the pinning and elastic energies [12,13]. However, this model is not able to predict or explain another conspicuous phenomenon: Usually, the motion of dislocations is not smooth, and they move in a jerky manner, resembling stick–slip processes. This is the result of the random pinning centers [9,14]. This situation was argued to be akin to a depinning transition, a statistical physics concept of an elastic manifold being driven through a random pinning potential [15,16]. The corresponding simulations predict rather complex avalanche-like dynamics with scale-free fluctuations in both space and time and even have been successfully used to describe earthquakes, domain wall motion in ferromagnets, vortices dynamics in type-II superconductors [17]. Such a model can be expected to also apply to dislocations in HEAs, because dislocations can be considered as elastic lines: the line tension tends to straighten curved dislocations to minimize elastic energy.

The avalanche-like motion of dislocations has been reported for pure metals mostly based on the compression of single crystalline micro- and nanopillars [18,19], nanoindentation [20–22] and acoustic emission measurements [23,24]. Apart from size effects [25,26], the most striking difference of micro- and nanoscale phenomena as compared to bulk deformation is that instead of a smooth mechanical material response, a wealth of abrupt plastic events occur. These show as strain bursts or stress drops in the stress–strain curves [27,28] and are caused by local avalanche-like redistribution of dislocations. There, the size of the avalanches is taken as the global plastic strain increments, which was found both by experiments and simulations to follow a scale-free distribution (power law) [29–32]. The scale-free avalanche statistics are important because ultimately, they show that small-scale dislocation plasticity is a complex system far from equilibrium, which, under certain circumstances, can even be classified to be in the same universality class as earthquakes.

In situ transmission electron microscopy (TEM) is an effective tool to observe dislocation activities in small volumes and has been extensively utilized to study small-scale plasticity [33,34]. However, so far, a direct and quantitative TEM analysis of dislocation avalanches was not possible: a single dislocation in conventional FCC metals moves very fast and is very difficult to track. Moreover, dislocation avalanches are always accompanied by complex dislocation microstructure evolution which in turn makes understanding the origin of critical behavior difficult. Dislocations in HEAs [7,9,13,35] provide a great opportunity to directly study avalanches for single dislocation since the high lattice friction slows down the dynamics considerably, and recent TEM experiments were indeed able to show the stick–slip motion of dislocations during glide [9,36,37]. However, a dislocation shape and avalanche analysis would require complete and accurate spatio-temporal information of the dislocation lines.

Up to date, a quantitative analysis of the dislocation structure and avalanche behavior from direct experimental observation of dislocations was not possible. In this work, we investigate the dynamics of individual dislocations in a HEA material. Our high-throughput, deep learning-based image analysis of *in situ* TEM data allows us to exactly reconstruct the spatio-temporal evolution of the dislocation microstructure and to report on direct experimental measurements of the stick–slip motion. It shows that critical behavior in the context of the depinning framework can already be manifest at the level of individual dislocations. Moreover, complementary discrete dislocation modeling is presented that, in addition to explaining the experimental findings, unveils the effect of fluctuations on the dislocation line roughness and the universal nature of the avalanche-like dynamics.

2. Methods

2.1. The in situ TEM experiment

In situ straining experiments were carried out on a Gatan low-temperature straining holder, using a JEOL 2010HC TEM equipped with a Mega view III CCD camera from the EMSIS company. This allows us to capture 23 images/s (46 frames/sec) that are converted in a 50 Hz video flux, which means that some images (about 2–3 per second) are combined frames that need to be ignored. This possible limitation only applies to fast dislocation movements such as those immediately preceding annihilation (fractions of a second). However, those are anyway not observable with this camera. Note that due to different loading stresses, there were roughly 4300 frames for the first experiment while only around 200 frames for annihilation experiment 3 and 4. The tensile sample preparation is described in [36]. Although compression is not possible with such a holder, the reversible loading of local parts of the specimen is possible because of the overall elastic loading of the ensemble of holder, frame, and sample. We meticulously focused on such a specific region of the specimen to obtain our *in situ* cyclic loading experiments, where we observed the phenomenon of dislocation annihilation. As shown in movie 1 (cf. Appendix A.2), the initial phase of the experiment revealed a slip trace area with distinct dislocation patterns: three dislocations were present in the left region, and one dislocation was observed in the right region. During the experiment, the three dislocations in the left region moved toward the right, while the single dislocation in the right region as shown in this particular frame of the video, moved toward the left. This movement led to the annihilation of these dislocations. The process of dislocation annihilation continued throughout the experiment.

All observations were obtained under a 200 kV electron beam while the sample was maintained at about 110 K. Such a low temperature, coupled with the bright LaB6 gun of the TEM and FCC structure of the alloy allowed the observation of thick regions of the specimen (up to 700 nm). The sample thickness in regions of interest was assessed through geometrical projection of the slip traces produced by dislocations on both surfaces of the foil. We used an elastic shear modulus of μ=84.65 GPa and a Burgers vector magnitude $b = 0.252\,46$ nm to infer the local stress acting on the curved dislocations. The complete crystallographic orientation of the region of annihilation, including the Burgers vector determination was done using two beam diffraction patterns acquired during the experiment and following the invisibility criterion ($\vec{g} \cdot \vec{b} = 0$ where $\vec{g}$ is the diffraction vector and $\vec{b}$ the Burgers vector) in two beam conditions. The Burgers vector direction was further confirmed by identifying cross-slip behavior between two indexed (111) slip planes.

2.2. Deep learning-based identification of dislocations

Typical deep learning approaches for binary segmentation of images consist of training a convolutional neural network which, if the training process was successful, results in a pixel-based image with the “mask”: black and white pixel where one type indicates the background and the other one the foreground, i.e., the dislocation. The methods are limited by the fact, that for the current analysis, dislocations are required as mathematical polynomials or splines. To avoid having to fit a spline to the pixelated masks we developed an approach for spline support points prediction using a Mask R-CNN. This directly predicts 20 support points on each dislocation, each of which consists of a pair of coordinates. These points can be used to obtain the spline without further postprocessing. To avoid having to manually annotate thousands of images as training data, we use our in-house developed synthetic data generation model described in detail in the previous work [38,39]. More details on the synthetic data and machine learning method are provided in Appendix B. As a result, the trained model is able to predict the mathematical dislocation lines from TEM images with very high precision (as is particularly important for the analysis of avalanches) and even in cases where nearby dislocations nearly overlap. To further increase the accuracy of predicting the position of dislocation lines to sub-pixel precision, the TEM images were processed prior to the training. For this purpose, classical image analysis methods such as image registration and keypoint stabilization were used, cf. Appendix C.

2.3. 3D DDD (static) simulations

To compute the stresses of dislocations inside a finite volume, the 3D Discrete Dislocation Dynamics (DDD) simulator MoDElib (Mechanics Of Defect Evolution Library) was used. MoDelib is an open-source code [40] which is based on discretizing curved dislocation lines into a series of connected segments. The simulation tool incorporates boundary conditions and image forces by merging solutions for an infinite domain with a Finite Element Method (FEM)-based boundary corrections. Further details about MoDElib are available in [41] and the references therein. The present work reconstructs dislocation configurations from Transmission Electron Microscopy images to a slip plane within a foil, of approximately 675 nm thickness, as illustrated in Fig. 4(b). The shear stresses acting on dislocations in general may arise from various sources: external stress, interactions among dislocations, dislocation self stresses, and image stresses due to free surfaces. All mentioned stress components together except for the external stress are here termed "internal stress". These stresses are calculated using the DDD model with Dirichlet boundary conditions on the foil's left and right surfaces, and traction-free conditions on all other boundaries. Our focus is on the shear stress associated with a stick–slip event. Therefore, to remedy the challenge of pinpointing the exact location of which part of the dislocation starts moving first, we estimated the average shear stress along the slip direction across the entire curved dislocation. This estimation is done by extracting stress data from the integration points along the dislocation segments.

2.4. 2D DDD (dynamic) simulations

To investigate the depinning of dislocations in a heterogeneous stress field, a 2D grid model was employed, based on [14]. The model mimics the motion of a single dislocation line in a glide plane due to an externally applied stress. It captures the elastic interactions between different parts of a moving dislocation line as well as the effects of the random local lattice distortions in a periodic domain. Values of the sites (i.e., the "grid points") are either 0 or 1, corresponding to plastic slip: the sites through which a dislocation line already passed take the value 1, and the others are 0. The contour between them represents the dislocation segments, which are either of edge or screw character. The resolved shear stress σ acting on a segment is the sum of the external stress σ_{ext}, the stress from the self-interaction of the dislocation σ_{self} (which includes the line tension), and the pinning field σ_{pin} (which represents the fluctuating lattice distortion of the HEA). The latter is an uncorrelated shear stress value assigned to every cell randomly drawn from a centered Gaussian distribution. The propagation of the dislocation line is modeled using random dynamics: at every time step a segment is chosen randomly, and the local resolved shear stress is calculated for that segment. Then the segment is moved in the direction of the glide component of the Peach–Koehler force. To study the stick–slip dynamics a loading protocol was employed where the external stress is increased gradually. During a slip event with a positive plastic strain increment, the stress drops. As a result, after a transient, the system reaches a steady state with a zig-zag like stress-time curve characteristic of stick–slip dynamics. The statistical analysis of dynamics and the shape of the dislocation lines were executed on the steady state regime of the simulations. A more detailed version of the model and the data analysis of the simulations can be found in Appendix D.2.

3. Results

3.1. Observations from the in situ TEM experiment

The *in-situ* TEM experiment was carried out on an equimolar CoCrFeMnNi FCC HEA (Cantor alloy) thin foil sample through a JEOL 2010 LaB_6 operating at 200 kV. The sample region of interest had a thickness

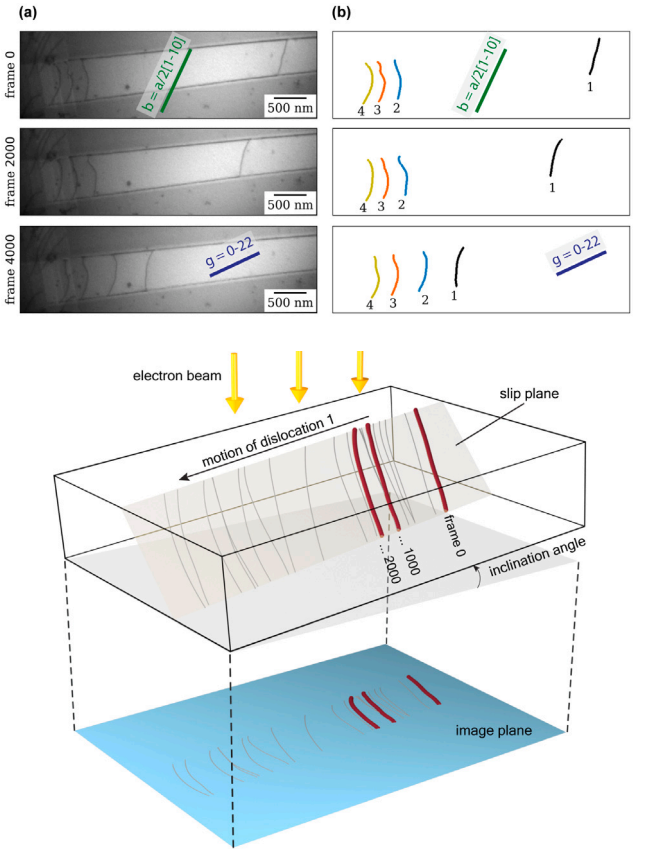

Fig. 1. Annihilation process #1: (a) Three typical TEM images including dislocations, recorded at equidistant time steps. The two roughly horizontal lines are slip traces. (b) Dislocation represented as splines obtained from a deep learning model. (c) Knowing the details of the crystallography allows us to reconstruct the dislocation shape in 3D space. The plot shows snapshots of the evolution of dislocation 1 at equidistant time steps during the whole experiment from the first appearance to the annihilation of the dislocation; the bottom projection shows this in the original image plane as in (a) and (b). The electron beam is directed downwards.

of around 600 nm, which is close to the maximum possible thickness in our setup. Further details are given in "methods" below and Appendix A. The experiments were designed such that only very few dislocations are present, where two of them have opposite Burgers vector directions. These dislocations are attracted and move toward each other until they annihilate. Altogether four experiments with such annihilation processes were performed which will be analyzed individually (cf. movies described in Appendix A.2).

Fig. 1(a) shows examples of TEM images obtained from one of the movies. There, dislocations appear as curved, line-like objects that terminate at the straight, nearly horizontal dark lines, the slip traces at the surface of the foil. These slip traces are not exactly parallel which results from the fact that the surfaces of the sample are not perfectly co-planar.

3.2. Image analysis

For extracting the position of the dislocations one could in principle use a software for manually annotating the images as, e.g., done in [37]. However, the accuracy may depend on the person who is performing this task and may vary from line to line. Additionally, this process is extremely time-consuming and cannot be manually done for thousands of frames. Classical image analysis approaches, on the other hand, typically fail due to the complexity of such images. Deep Learning models trained on synthetic data turned out to be efficient and accurate

alternatives. The model resulting from the "general training" can be kept and only needs to be fine tuned with 10..50 images for the new situation. Allowing this easy transferability was one of the pragmatic goals of our strategy (more details are given in the section "Methods" and the Appendix B): dislocations represented as mathematical polynomials can then be used to calculate geometrical properties such as the dislocation curvature or orientation. Subsequently, the information about the orientation of the sample and crystallographic directions were used to reconstruct the 3D dislocation lines from their 2D projections. Fig. 1(c) shows this for dislocation 1 and several different frames of the first annihilation experiment. It is observed that the propagation of the dislocations is not homogeneous, and the uneven spacing between the lines is a signature of small strain bursts. (cf. supplementary movies described in Appendix A.2).

3.3. Detection of strain bursts

To quantify the characteristics of the dislocation motion, the rightmost dislocation number 1 was automatically tracked for all 4 annihilation experiments. Fig. 2(b) shows this dislocation for each frame during the first experiment. Clearly, the propagation of the dislocation line is jerky, forming "islands" of various sizes between subsequent frames that correspond to the individual dislocation avalanche events. Fig. 2(a) sketches such an island between two subsequent time steps t_i and t_{i+1} with $\Delta t = t_{i+1} - t_i$. The area ΔA_i swept by the dislocation within the slip plane was numerically calculated and is associated with a dislocation avalanche; it is proportional to the plastic strain increment caused by the event. The proportionality factor depends on the Burgers vector and sample geometry. Since the latter is not known with sufficient accuracy, we identify the size of the events S with the slipped area ΔA_i because as long as scale-free features are concerned, a multiplicative factor is irrelevant. Fig. 2(c) shows the swept area increment and the accumulated area as a function of the movies' frame number. The high fluctuations are due to the jerkiness of the dislocation motion.

3.4. Dislocation avalanche statistics

The statistical distribution of the sizes S of individual avalanches of the rightmost dislocation were analyzed. This was done for the four consecutive annihilation experiments; the distributions of the avalanches were found to follow the scale-free distribution $P(S) \propto S^{-\tau} C(S/S_0)$, where τ is the avalanche exponent, S_0 is a cut-off and C is a cut-off function that decays faster than algebraically for large arguments [28]. Fig. 3 shows the distribution of avalanche sizes (i.e., the swept area). Consistent with depinning, the avalanche statistics follow a power law distribution that holds for roughly four orders of magnitude of the avalanche size S without any apparent cut-off. The exponents for the different annihilation processes take values in the range $\tau = 1.05 \pm 0.05$.

As shown in Fig. 2(b), during a plastic event typically only a section of the dislocation line moves. To explore further scale-invariant features of the dislocation motion, the shape of these slipped island-like areas of individual events was analyzed. In particular, the dependency of the size of the slipped area S w.r.t. the avalanche width w was analyzed. According to depinning theory, the slipped areas are expected to be self-affine, i.e., $S \propto w^{1+\zeta_{av}}$, where ζ_{av} is the avalanche roughness exponent. Fig. 3(b) demonstrates that this relationship holds indeed with $\zeta_{av} = 0.34 \pm 0.05$.

3.5. Influence of the loading

In small-scale crystal plasticity, an often observed aspect of the respective universality class is a dependency of the avalanche statistics on the loading, i.e., type and magnitude. The underlying reasons are attributed to mechanisms such as localization versus self-organization (e.g., [42]) or stress inhomogeneities (e.g., [43]). To understand if in the case of single dislocation avalanches the dependency on the loading should be understood as a type of self-organized criticality, as suggested by the occurrence of power laws, we investigate the correlation between the driving stress and the avalanche size [44].

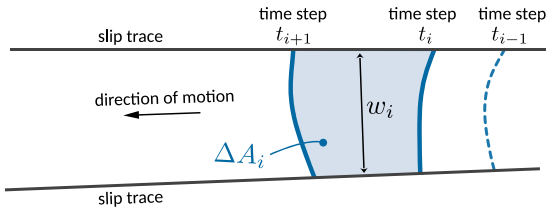

(a) sketch of the dislocation motion and slipped area

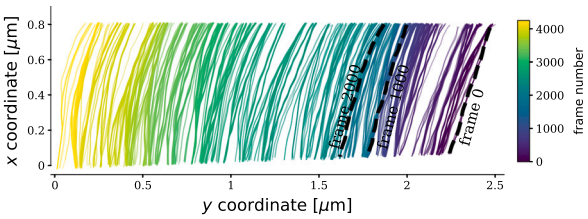

(b) superposition of all frames

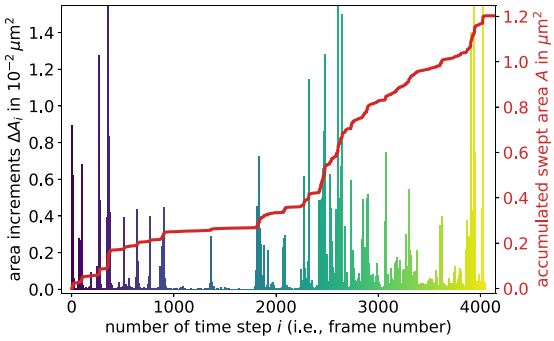

(c) area increments and accumulated area

Fig. 2. **(a)** Visualization of the dislocation's swept area per time step (light blue shaded area) from which the average velocity can be obtained. **(b)** The shape of dislocation 1 during annihilation process #1 as extracted by the ML algorithm. The colors indicate the frame nr, that is, the elapsed time. **(c)** total swept area of dislocation 1 (red) and increment of swept area for each frame (blue). The noisy character of the curve comprising of peaks of random size is an indicator of jerky motion. (For interpretation of the references to color in this figure legend, the reader is referred to the web version of this article.)

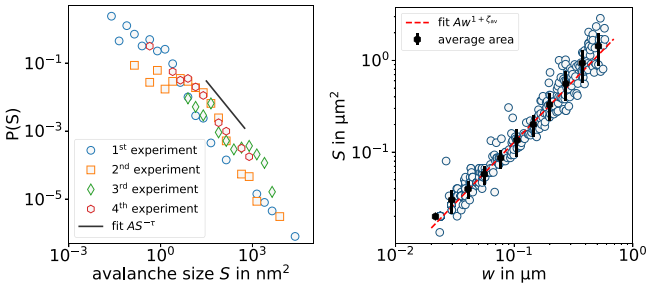

(a) avalanche statistics (b) line roughness

Fig. 3. **Scale-free properties of experimentally observed dislocation avalanches.** The avalanche exponent τ of the power law distributions in (a) is $\tau = 1.05 \pm 0.05$. Avalanche sizes smaller than the area of a quarter of a pixel are not considered. Panel (b) shows the size S vs. width w of each avalanche, and the fitting gives the roughness exponent with a value of $\zeta_{av} = 0.34 \pm 0.05$.

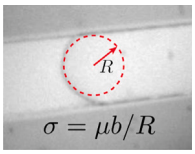

(a) sketch of how the excess stress is estimated in the slip plane

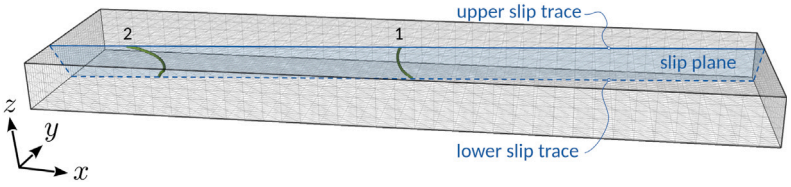

(b) DDD simulation setup for obtaining internal stress

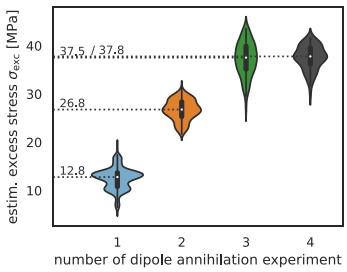

(c) excess stress for all experiments

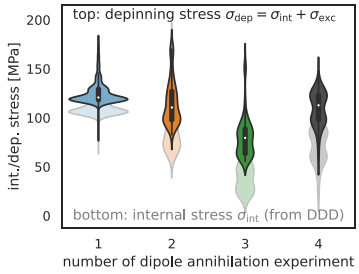

(d) internal stress and depinning stress

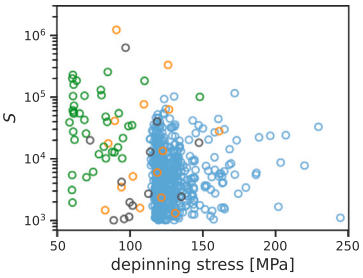

(e) depinning stress vs. avalanche size

Fig. 4. Shear stresses during dislocation avalanches. (a) The excess stress in the slip plane is estimated using a line tension approximation. (b) 3D reconstruction of a dislocation configuration used as the initial values for a 3D DDD model for calculating the internal stress, i.e., the shear stress due to dislocation interactions and boundary conditions. The "violin plot" in (c) visualizes the distribution of excess stress obtained from (a), the dotted lines indicate the median of each distribution. The violin plot in (d) shows the distribution of internal stress (the light-colored, lower distributions) as obtained from (b) and the depinning stress (the dark plots in the upper row). The differences between the two overlapping rows of plots are the excess stresses. (e) Relation between the shear stress acting on a dislocation and the avalanche size obtained as the slipped area.

The shear stress acting on a short segment of a dislocation consists of a component from the applied external loading, σ_{ext}, a friction-like contribution due to the large local random lattice distortions of the HEA, σ_{fric}, and an internal stress, σ_{int}, due to interaction with other dislocations, the free surfaces, and possibly with other parts of the same dislocation. The applied external stress is not directly accessible from the *in situ* TEM straining experiment.

A commonly used strategy to estimate this stress is based on the assumption that in an equilibrium situation, the external stress is balanced by the line tension [45] such that $\sigma_{ext} \approx \mu b/R$ where R is the radius of curvature of the dislocation and μ is the shear modulus. However, this expression is only valid, when a dislocation (i) bows out between two *strong* pinning points and (ii) the friction stress is negligible, $\sigma_{fric} \ll \sigma_{ext}$. This is typically the case in FCC materials due to the planar nature of the dislocation core.

In HEAs, however, due to large lattice distortion and interactions among multiple principal atomic species, the faces of the dislocation core are atomically rugged – as is the energy landscape – possibly resulting in an additional friction [46]. For a strong friction force, it is, thus, $\sigma_{ext} \approx \sigma_{fric} + \mu b/R$, i.e., the line tension $\sigma_{lt} = \mu b/R$ is an excess stress required to move the dislocation line due to pinning effects at the sample surface. σ_{lt} was obtained from fitting a circle to the line in the local slip plane coordinates, as obtained from the digitized and 3D reconstructed dislocation microstructure (see [37] and the Appendix). There, the surface-near regions of the line were ignored to avoid the influence of image forces. Fig. 4(a) shows a sketch of how the excess stress was obtained.

The resulting distributions of the excess stress are visualized in Fig. 4(c) (the width of the violin plots at a specific stress value indicates the frequency of that stress value similar to a histogram). The obtained values are significantly smaller than the critical resolved shear stress of this material, i.e., around 160 MPa at the given temperature (see Appendix D.4 for details). The average excess stress initially increases and then saturates during the sequence of the four experiments, likely due to history effects on the sample surface (note that the external stress is constant throughout each of the four experiments, but is different for each experiment).

For obtaining the contribution of σ_{int} the 3D reconstructed dislocation microstructure of all 5130 frames was used as input for a 3D DDD simulation. However, the DDD model was only used to calculate the internal stress; no dynamical simulations were performed (see the section"Method" below). Fig. 4(b) shows the model of the sample with two dislocations.

The corresponding depinning stresses include both the excess and the internal stress. Additionally, only those data points were considered that have a corresponding non-zero velocity, resulting in Fig. 4d for the four annihilation processes.

Fig. 4(e) shows that the depinning stress and the avalanche size are not strongly correlated. One can observe that the pinning forces acting on moving dislocations show significant fluctuations. This agrees well with a recent study of dislocation pinning in HEA [37]. Quantifying the strength of the relation between stress and velocity using Pearson's correlation coefficient for the stress and the avalanche size gives the values 0.07, −0.16, −0.02, and −0.12 for the four experiments, indicating that there is no correlation between the two variables.

The relation between the avalanche size and the depinning stress additionally emphasizes the difference between moving dislocations and other systems (such as fluid flow in porous media, or the dynamics of vortices in superconductors): in such a non-equilibrium system if the critical point is approached, then the intermittent behavior becomes associated with static random "obstacles" which exert space-dependent pinning forces on the moving objects [27]. Single dislocation avalanches exhibit the characteristics of self-organized criticality instead of stress-tuned criticality.

3.6. Interpretation in terms of 2D DDD simulations

The experimentally obtained power law avalanche statistics and the self-affine avalanche roughness exhibit robust scaling exponent characteristics of the stick–slip dislocation motion. However, the roughness exponent ζ_{av} is rather different from those predicted by dislocation-based models of depinning where ζ_{av} is in the range of $1.0 \sim 1.25$ (see Appendix D.6 for more details).

To investigate and explain the experimental findings, a 2D DDD model was employed which is based on [14] (see "Methods" and

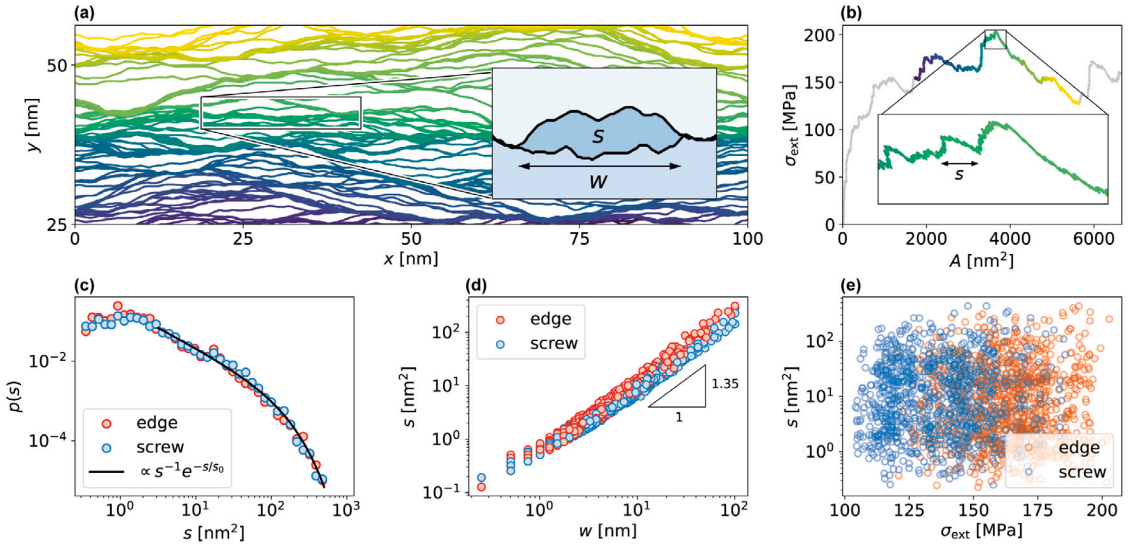

Fig. 5. 2D DDD modeling of single dislocation avalanche. (a): Dislocation during the steady state stick–slip motion along y-direction. The line is initially of edge character and parallel to the x-axis. The inset shows a magnified view of an event of size s and width w surrounded by the dislocation in its two consecutive metastable positions. **(b)**: Stress-slipped surface curve corresponding to the dislocation in (a). Plastic events correspond to the simultaneous drop of stress σ_{ext} and the increase of slipped surface A. These events are connected by quiescent periods characterized by increasing stress and constant A. The latter periods are marked by the colors of the corresponding stationary dislocation line in panel (a). **(c)**: Distribution of the avalanche sizes s for dislocations of both edge and screw characters and the fitted scale-free distribution with $\tau = 1$. **(d)**: Scatter plot of the slipped surface s versus the width w of the slipped region (see inset of panel (a)) for all plastic events. The data are consistent with $s \propto w^{1+\zeta_{\text{av}}}$ with $\zeta_{\text{av}} = 0.35 \pm 0.03$. **(e)**: Scatter plot between the applied stress σ_{ext} at the onset of an event and the size s of that event. The two quantities have a very low Pearson correlation of $C \approx 0.15$.

Appendix D for further details). The results of the simulations are summarized in Fig. 5. Panel (a) shows the propagation of the dislocation line through a sequence of metastable states. The slipped surface-stress curve in Fig. 5(b) exhibits a zig-zag pattern characteristic for stick–slip dynamics. Separate slip events were identified by thresholding the slipped surface rate. The distribution of slip sizes (slipped areas) obeys a power law with the same exponent $\tau = 1 \pm 0.05$ as in the experiments and with an exponential cutoff (panel (c)). In Appendix D.5 it is shown that the exponent τ is robust w.r.t. change of the dislocation character and to the typical obstacle strength in the material. The slipped surface S of slip events scales with the width w of slip events according to $S \propto w^{1+\zeta_{\text{av}}}$ where $\zeta_{\text{av}} = 0.35 \pm 0.03$ (panel (d)), in agreement with our experimental result in Fig. 3(b). To understand why ζ_{av} is different from the roughness exponents of the whole dislocation line ζ reported in the literature, we repeated the standard analysis by calculating the mean power spectrum of the dislocation lines and obtain $\zeta = 0.85 \pm 0.05$ (see Fig. D.11), which is very close to the values obtained above and in accordance with the scaling relation (Eq. (D.5)).

These findings imply that during an event, the height h of the slipped area increases (on average) much slower than the width w. Indeed, Fig. D.10 confirms this for both edge and screw dislocations by plotting the evolution of these quantities during an event. This means that a dislocation avalanche can be roughly envisaged as a forward propagation of a short dislocation segment followed by the lateral extension of the slipped area. The reason for this behavior is likely the anisotropic nature of dislocation self-interactions, as detailed in "Methods" and Appendix D.

Finally, Fig. 5(e) demonstrates that the simulated dislocation avalanches possess the same critical nature as in the experiments (Fig. 4(e)): The slipped surfaces (and therefore the plastic strain increment) during individual events are practically uncorrelated with the external stress.

4. Conclusion and outlook

We performed *in situ* TEM experiments of Cantor HEAs at low temperature and observed the non-smooth, stick–slip motion of individual dislocations. Through a high-throughput, deep learning-based extraction of dislocations as mathematical splines, we managed to reconstruct the shape and position of the dislocations in 3D with very high accuracy. Analyzing the stick–slip motion of dislocations by considering thousands of TEM images allowed us to obtain robust "single dislocation" avalanche statistics which exhibit strong evidence of power-law statistics. The exponent of the distribution shows independence on the external driving stress which is a clear feature that distinguishes dislocation plasticity from other disordered, non-equilibrium systems. Our phenomenological 2D DDD simulations confirmed the power law statistics of single dislocation avalanches and additionally reveals that long range interactions as the main source of interactions in this model are essential.

The microscopy work itself is already a novelty due to the detailed observation of the dislocation motion. However, the most intriguing aspect of this work is the combination of dedicated experiments with a novel data mining strategy for analyzing large amounts of *in situ* TEM data. Until recently, it has not been possible to analyze *in situ* TEM data in such a quantitative manner, let alone to observe and analyze avalanche behavior or to interpret it in terms of simulations.

We see this work as a critical step toward a transformed materials science community, where data science and artificial intelligence approaches in combination with tailored experiments and microscopy help to truly bridge the gap to simulations and to allow the extraction of knowledge that otherwise would remain hidden.

CRediT authorship contribution statement

Hengxu Song: Writing – review & editing, Writing – original draft, Software, Formal analysis. **Binh Duong Nguyen:** Writing – review & editing, Writing – original draft, Visualization, Software, Formal analysis. **Kishan Govind:** Writing – review & editing, Software, Formal analysis. **Dénes Berta:** Writing – review & editing, Software, Formal analysis. **Péter Dusán Ispánovity:** Writing – review & editing, Software, Formal analysis. **Marc Legros:** Writing – review & editing, Resources, Funding acquisition, Formal analysis. **Stefan Sandfeld:** Writing – review & editing, Writing – original draft, Visualization, Supervision, Software, Funding acquisition, Formal analysis, Conceptualization.

Code availability

The trained deep learning model along with analysis code (Python), as well as the scripts for reproducing the figures, is openly available at https://gitlab.com/computational-materials-science/public/publication-data-and-code/2024_in-situ_tem_avalanches where additional updates are provided. A snapshot of this repository from the publication date is also published on Zenodo: https://zenodo.org/doi/10.5281/zenodo.10800695. The code for the 2D DDD simulations can be obtained from https://github.com/bertadns/DDS.

Declaration of competing interest

The authors declare that they have no known competing financial interests or personal relationships that could have appeared to influence the work reported in this paper.

Acknowledgments

This work was primarily financed by the European Research Council through the ERC Grant Agreement No. 759 419 MuDiLingo ('A Multiscale Dislocation Language for Data-Driven Materials Science') led by S. Sandfeld and M. Legros.

Additionally, H.S. acknowledges the financial support from the Strategic Priority Research Program of the Chinese Academy of Sciences (Grant No. XDB0620101). D.B. and P.D.I acknowledge financial support from the National Research, Development and Innovation Fund of Hungary under the young researchers' excellence program NKFIH-FK-138975, from the Ministry of Innovation and Technology of Hungary from the National Research, Development and Innovation Fund, financed under the ELTE TKP 2021-NKTA-62 funding scheme, and from the European Union project RRF-2.3.1-21-2022-00004 within the framework of the MILAB Artificial Intelligence National Laboratory. D.B. was supported by the EKÖP-24 University Excellence Scholarship Program of the Ministry for Culture and Innovation from the source of the National Research, Development and Innovation Fund. The authors thank Antonin Dlouhy from CEITEC IPM, Czech Academy of Sciences, Brno, Czech Republic, for providing the Cantor alloy. Last but not least, we would like to acknowledge helpful discussions with Lasse Laurson and Joachim Mayer. We are additionally grateful to Giacomo Po for support with the open source code "MoDELib" [40].

Appendix A. Additional information for experiments

A.1. Parameters

Table A.1 shows all parameters that are required for the three-dimensional reconstruction of the dislocation lines from the two-dimensional images.

The foil thickness t at the location of the annihilation is calculated from the slip traces of the dislocations gliding in the (111) plane. The projected distance between the slip lines t_{proj} varies between 600 and 700 nm. The corresponding (111) plane is inclined by an angle of 50° from the horizontal/camera plane for the given Euler angles. The local calculated thickness t is therefore

$$t = t_{\text{proj}} \tan 50^\circ ,$$

which results in a value range of 715–830 nm. Observations in such thick regions of the foils are facilitated by the low temperature experiment.

Table A.1
Parameters of interest from the TEM experiment.

Symbol	Definition	Value
(ϕ_1, Φ, ϕ_2)	Bunge Euler angles	$(59.1^\circ, 80.2^\circ, 92.3^\circ)$
$\boldsymbol{n}$	Slip plane normal	$[1, 1, 1]$
$\boldsymbol{b}$	Burgers vector	$(1, -1, 0)$
θ	Tilt	5°
T	Temperature	108.13 K

A.2. Supplementary movies of the in situ TEM experiment

There is one movie for each of the four annihilation experiments (`supplementary movie #1 – #4`):

- Movie #1: There are roughly 4200 frames. Each frame consists of 4 dislocations: three dislocations from the left move toward the right and one dislocation from the right moves toward the left.
- Movie #2: There are roughly 700 frames. Each frame consists of 3 dislocations: two dislocations from the left move toward the right and one dislocation from the right moves toward the left.
- Movie #3: There are roughly 200 frames. Each frame consists of 2 dislocations: one dislocation from the left move toward the right and one dislocation from the right moves toward the left.
- Movie #4: There are roughly 120 frames. Each frame consists of 2 dislocations: one dislocation from the left move toward the right and one dislocation from the right moves toward the left.

Appendix B. Deep learning-based image analysis

Dislocation information exists in sequences of bright/dark field images where one can extract dislocation information (coordinates) through segmentation. This segmentation task is usually done by manually labeling the dislocation lines. Unfortunately, this requires expert knowledge and is too tedious to be feasible for actual experimental data consisting of several thousand frames.

Ever since the seminal work of Krizhevsky et al. [47] deep learning (DL) has had a tremendous impact on image processing in materials science or microscopy. Various improved deep neural networks have been developed, such as ResNet for classification and U-Net for segmentation. However, the predictive ability/accuracy of these neural networks is greatly limited by appropriate training data when solving real-world problems. Especially for transmission electron microscopy (TEM) images of dislocations, the difficulty originates from the collection of a large number of high-quality TEM images (for training) and accurately labeled dislocations in the images containing other objects such as grain boundaries, slip traces, and even image noises. Synthetic data can easily solve the limitation of data collection. However, high-quality data also requires the proper/correct physical features encoded in the generated synthetic data. Recently, Govind et al. [38] proposed a parameter-based synthetic data generation model to generate synthetic training data (images and ground truths) for a number of machine learning approaches i.e., dislocation segmentation, instance segmentation, dislocation spline support point estimation. A machine learning (ML) model trained on such synthetic data is able to exclusively extract dislocation segments from TEM images.

In this work, we use a keypoint detection approach based on the Mask R-CNN [48] architecture to obtain support points on the dislocations directly, which can be used to represent a dislocation as a spline (i.e., a piecewise polynomial). We found that 20 points on a dislocation are sufficient to accurately obtain a spline representation of a dislocation. We use the Mask R-CNN model developed in the Pytorch framework with a ResNet50 as backbone and inherit pre-trained weights, which are obtained by training the backbone for image classification problems on the ImageNet [49] dataset.

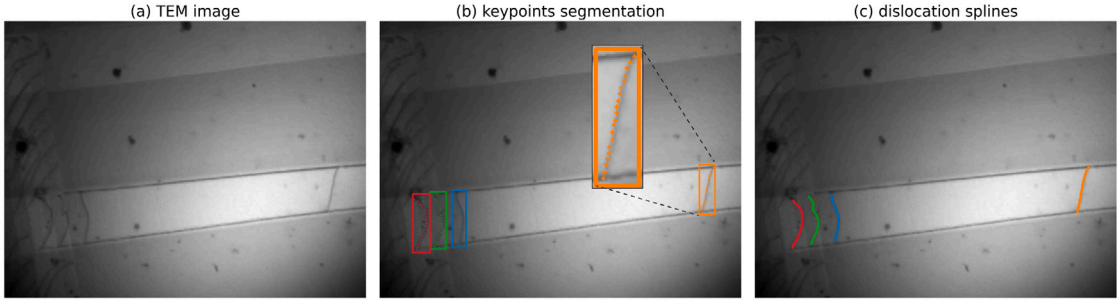

Fig. B.1. Identification of Dislocations. The left panel shows a frame from the experiment showing the dislocations part of the annihilation process. Middle panel: 20 keypoints on each dislocation are identified by the deep learning model, acting as support points for splines (i.e., piecewise polynomials), as shown in the right panel. Based on these splines, it becomes straightforward to compute, e.g., the local curvature of dislocations.

B.1. Keypoint detection

The keypoint detection method represents a distinct approach in dislocation image analysis compared to binary and instance segmentation by directly identifying "key points" on the dislocation line. This method is similar to pose detection, where algorithms detect and mark various body parts (such as the head, hands, elbows, legs, and toes). In the context of TEM dislocation images, keypoint detection algorithms are trained to pinpoint points on the dislocations, which can be used as support points to represent the dislocations as shown in Fig. B.1. The primary advantage of keypoint detection lies in its direct approach. It eliminates the need for the intensive post-processing required in segmentation methods. It simplifies the process of generating spline representations by directly providing support points for dislocations. This can lead to a more efficient analysis process, especially in cases where rapid processing is essential. However, keypoint detection is challenging. The accuracy of this method hinges on the precise identification of keypoints, which requires a robust and well-trained model. The complexity increases with the density and intricacy of dislocation networks in the images. Ensuring that the detected keypoints accurately represent the dislocation structure is crucial, as misidentification can lead to incorrect analysis of the dislocation characteristics.

B.2. Synthetic datasets training

Generating a synthetic dataset with a parametric model requires incorporating several parameters that represent aspects of the image background and geometrical properties of the dislocation lines. Examples for the former are the degree of noise in the background or the occurrence of larger image artifacts, examples for the latter are the number, shape, and orientation of the dislocations. Furthermore, for the numerical approximation of the dislocations in form of splines, the support points on the dislocation lines are required. These points are essential in modeling dislocations as splines within synthetic microstructures. Based on our previous work in [50] we established a comprehensive database of typical line shapes derived from 70 distinct real dislocations and recorded the most suitable, corresponding support points for approximating these dislocations. Furthermore, the synthesis of this dataset involves the integration of several additional parameters (i.e. number of dislocations, number of pileups, slip width, dislocation spacing and slip direction of pileup). Statistical analysis of a range of TEM images from different experiments (including experiments from a large literature base) was performed to establish a general value range for all parameters, which enables the generation of diverse synthetic images. The current work only requires specialized situations which, however, are also covered by described, more general approach. The images exhibit variations in microstructure, contrast, and pixel intensity. It is worth noticing that some structures such as slip trace lines can easily be incorrectly predicted as dislocations. In this work, we have also explicitly included slip trace lines in the synthetic data to help the model learn and distinguish them from dislocations. In particularly, this is useful for the here investigated TEM image dataset which contains distinct slip trace showing as darker lines.

B.3. Training and validation

We train the Mask R-CNN model on 5000 synthetic image data to predict 20 support points on each dislocation. Examples of some synthetic images are given in Fig. B.2. Generally, the dataset consists of images with relatively simple microstructures (e.g., Fig. B.2a and b), which have dislocation pileups with non-overlapping or intersecting lines, as well as more complex microstructures (e.g., Fig. B.2c and d) where dislocation pileups overlap. Furthermore, we also have dislocation microstructures with slip trace lines. It is important to note that the synthetic dislocation microstructures are not based on any physical models and hence might not represent any realistic microstructure, but nonetheless, such microstructures provide a diverse range of microstructures to train the models improving the robustness of the models.

The comparison of synthetic images (as those shown in Fig. B.2) with real experimental images (as shown in Fig. B.1) reveals a clear difference between the two types. Real and synthetic images often differ significantly in terms of texture, noise patterns, lighting conditions, and other subtle characteristics. These differences can lead to a disparity in the model's performance, as it may not have learned to cope with the intricacies present in real experimental images. Furthermore, synthetic data often lacks the noise and imperfections that exist in real experimental data, which can be a challenge with the prediction capabilities. During the training of the model on synthetic images, we apply several image transformation methods such as Gaussian noise, Clahe, brightness contrast, etc. However, the synthetic data still has a lower feature variance and might not be able to provide high-quality results when used for prediction on real images. The key is to complement synthetic data with real experimental data to ensure the model is robust, versatile, and capable of generalizing well to real-world scenarios (see below).

The predictions on some of the synthetic images are shown in Fig. B.2. There, we observe that the trained model was able to accurately predict the support points on the dislocations, especially on the simple dislocation microstructures such as Fig. B.2a and Fig. B.2b where dislocations do not overlap or intersect each other. On careful observation we find that even though in the synthetic datasets we have equally spaced spline support points, in the predictions this is not always the case as seen for dislocation marked D1 in Fig. B.2b. The spline might be incomplete in case the model fails to predict the dislocation endpoint. The model was successful in distinguishing between slip trace lines and dislocations. Even for dislocations with sub-pixel spacing (i.e., lines that overlap) it was still able to assign the support points to the dislocations accurately. This is one of the unique features of this approach where the model is capable of predicting

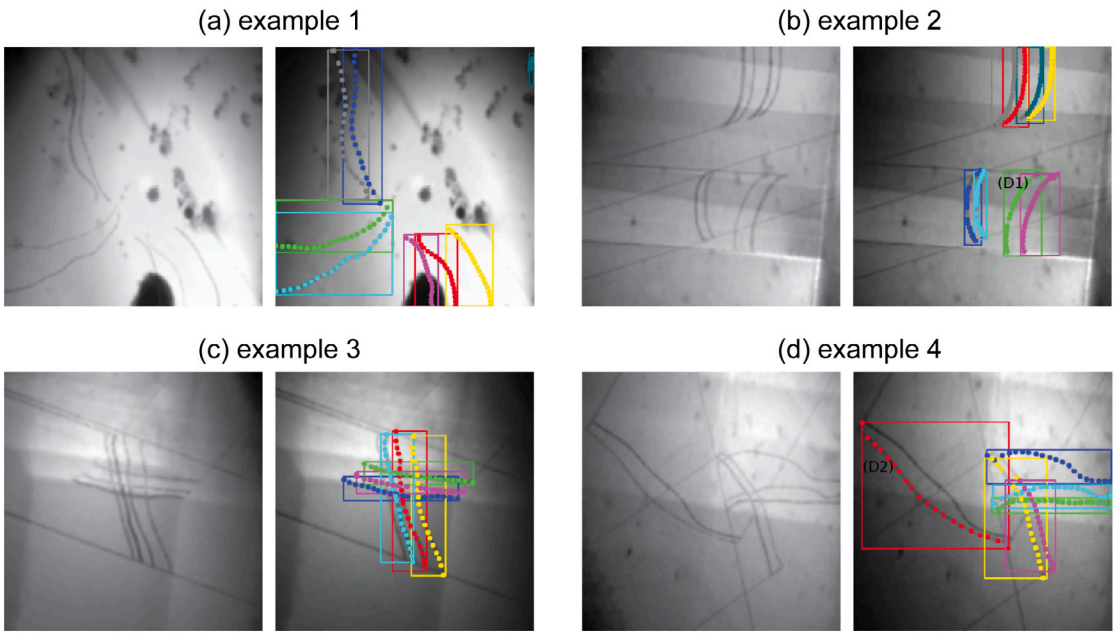

Fig. B.2. Synthetic images and predictions. Each of the four examples shows the synthetic image on the left together with the predictions of the Mask R-CNN model on the right. The model was only trained with synthetic data. The predictions consist of pairs of bounding box and keypoints. The examples in (c) and (d) are very complex due to intersecting lines. The DL model still performs very well.

such dislocations. This makes it much more suitable in particular for dislocation segmentation as compared to all commonly used CNN-based approaches. The predictive power of the model is somewhat reduced, however, when dislocations in an image strongly overlap and intersect each other (e.g., shown in Fig. B.2c and d). In such cases, we find that either the model fails to predict dislocations on the complete dislocations or predicts some of the points on the neighboring dislocations.

B.4. Fine-tuning with real image data

As shown in the second column of Fig. B.3 the model trained only on synthetic data is able to make predictions but the results are not of highest accuracy. There are two main issues: The first issue is that the model was trained to predict *all* dislocations present in an image – and hence the model also predicts those dislocations that are not part of the slip plane of interest as can be seen in Fig. B.3b and k. The second issue is much more critical as the model fails to predict dislocations of interest (Fig. B.3b and k). Both issues are very common when a machine learning model is trained on a dataset of a "synthetic domain" and evaluated on a dataset of a "real domain" – despite the use of data augmentation methods as a remedy to improve the domain generalization of the model trained on the synthetic dataset.

To increase the accuracy of the predictions for the whole dataset, we have further fine-tuned the model with a subsequent training with 10 images from each of the four experiments. For the training, we have hand-labeled these images where we marked only those dislocations that are part of the slip region of interest. Fine-tuning is done by a sequence of two training steps: it starts with training the whole model with synthetic images, followed by training of only the "head" of the network with only a few real, hand-labeled images. During this step only the weights of the last part of the network are trained, all other weights are "frozen". Note, that already the first steps also starts with a pre-trained model, using generic weights from the ImageNet.

The results for this approach are shown in the third column of Fig. B.3. It is remarkable to see that even though we used only 40 images to fine-tune the model, we obtained significantly better results. Additionally, it turned out that training on synthetic images has the benefit that the labels do not exhibit the human bias introduced during hand-labeling. We observed in a study (not shown here) that the use of synthetic images significantly helps to learn even small fluctuations in the line geometry – as is very important for, e.g., computing the curvature as required for this work.

Appendix C. Image analysis: Video stabilization and spline preprocessing

C.1. Video stabilization and dislocation spline preprocessing

Due to the impact of the environment (noise, vibrations) on the recording of the experiment a range of oscillation or of (more or less) random shifts of the image may take place. Therefore, to guarantee a high precision of the three-dimensional reconstruction and determination of the dislocation position, it is necessary to perform video stabilization before further analysis. We automate this process by writing a Python code with the library package openCV [51]. The video recorded from the four experiments are converted into frames (i.e., individual images). The experiments 1–4 contain four consecutive annihilation processes, which consist of roughly 4200, 700, 200 and 120 frames, respectively. All images undergo a contrast enhancement process to reveal most of the important features of the image. For each of the four annihilation process, we chose a fixed frame, to which we transform other frames. We first find keypoints and descriptors from this chosen frame using SIFT (scale-invariant feature transform) from openCV (see Fig. C.4a). Note, that here "keypoints" refers to reference feature present in all images and *not* the points on the dislocation, extracted by the DL model. SIFT [52] transforms the image into a set of feature vectors, which consist of keypoints and descriptors, and they are invariant to image transformations (such as translation, scaling, or rotation). The Lucas–Kanade method [53] (also implemented in openCV) is then applied to track the motion of these keypoints for every frame with this fixed original frame. This method uses the least squares criterion to solve the optical flow equation, assuming that the flow is constant in the vicinity of the considered point. At the end, it returns the estimated position of these keypoints in every frame. With the two sets of points, one from the original frame and one from the

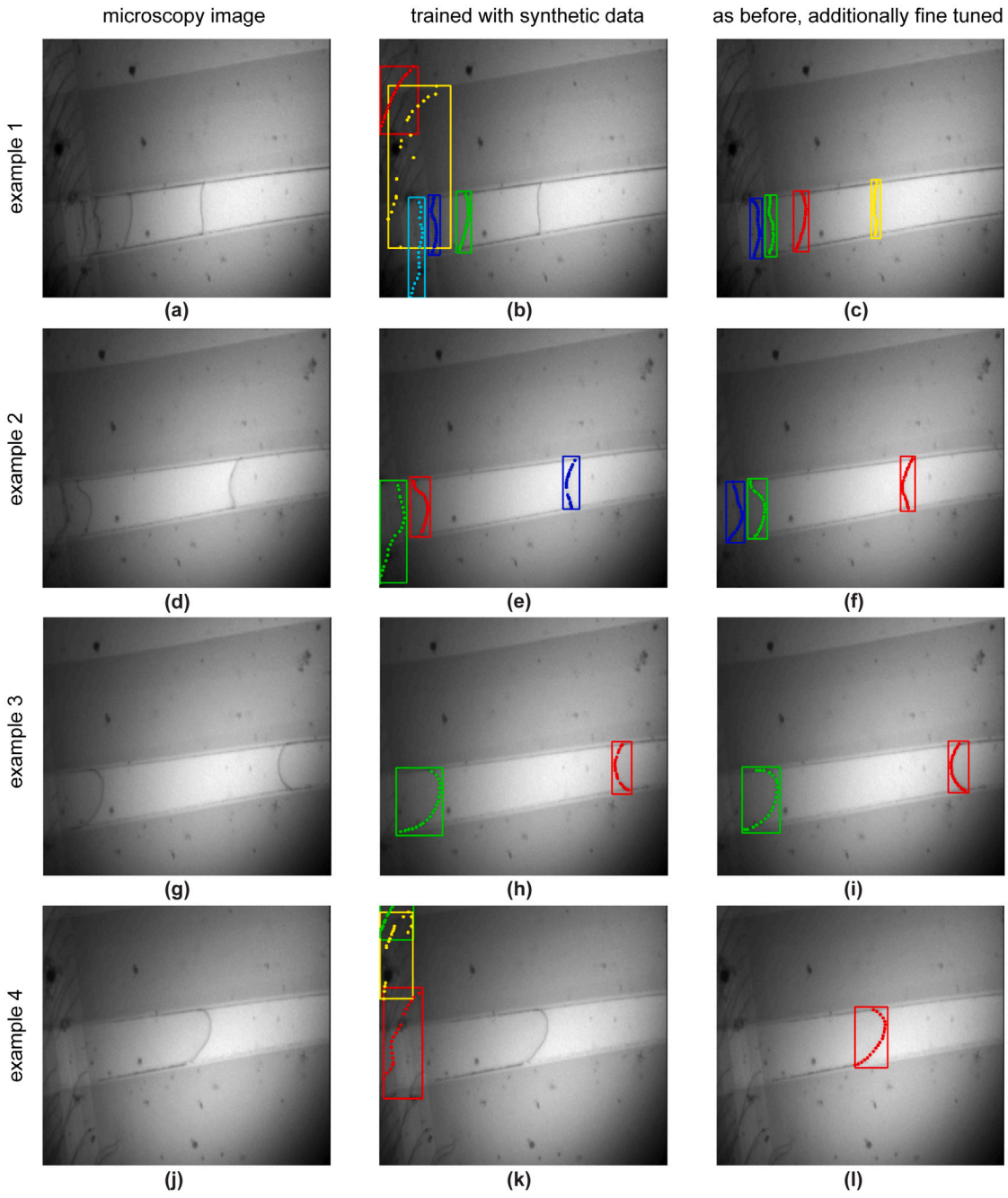

Fig. B.3. Training with synthetic data and additional fine-tuning. The left column shows an image from each of the four experimental videos. The middle column shows the corresponding predictions from a model trained only on synthetic data, while the right column shows the predictions with a model that was additionally fine-tuned with a few real images.

distorted frame, we can find the 2D affine transformation (four degrees of freedom) matrix as,

$$H = \begin{bmatrix} \cos(\theta)s & -\sin(\theta)s & d_x \\ \sin(\theta)s & \cos(\theta)s & d_y \end{bmatrix}, \tag{C.1}$$

where θ is the rotation angle, s is the scaling factor and d_x, d_y are translations in x and y axes. This matrix is used to warp the distorted frame back to the original frame, which is shown in Figs. C.4b and C.4c where for visualization purposes two frames from one of the movies were superimposed, indicated by the two different colors. It can be observed, that there is a significant difference between the original and transformed frames, demonstrating that this type of image postprocessing is crucial for the whole data analysis pipeline and that it needs to be conducted with greatest possible accuracy.

In principle these images are now ready to be used with the trained deep learning model. However, it turned out that the accuracy is enhanced if an other approach is used:

1. the deep learning predictions are performed on the original images
2. this result in dislocation keypoints (these are the points on the lines)
3. we use the matrix from Eq. (C.1) to transform the dislocation keypoints (see Fig. C.5a and b)
4. finally, a spline is fitted to these transformed dislocation points.

The effect of the transformation can be see in Fig. C.5 which shows the dislocation of interest from all frames. The reason why

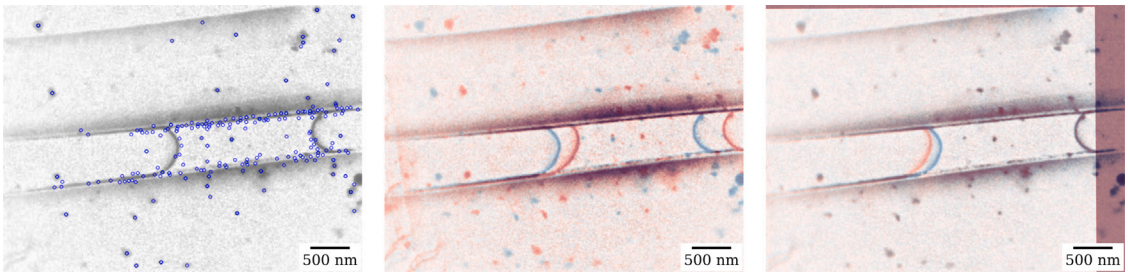

(a) important dectected keypoints (b) original, unwarped frames (c) warped frames

Fig. C.4. Visualization of the video stabilization process. The two colors indicate two subsequent frames, extracted from one of the videos. Keypoints in this context are, e.g., small impurities or defects on the surface of the material that are present in all images.

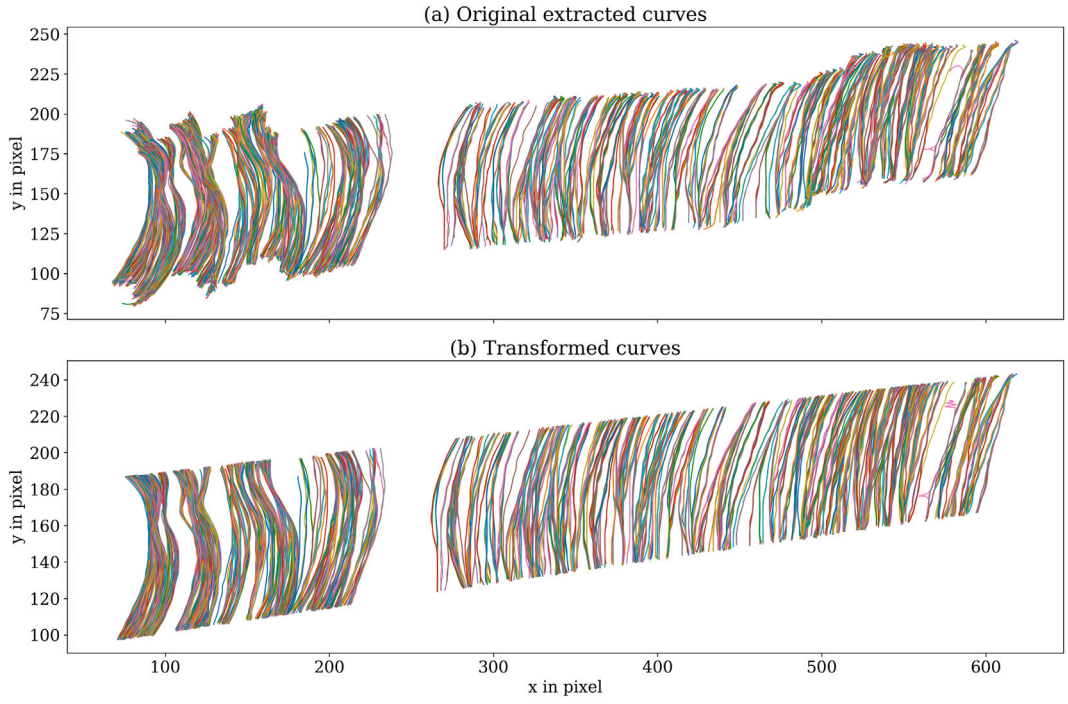

Fig. C.5. The superposition of all four dislocation in experiment 1 from all frames shows the impact of the stabilization on the extracted dislocation curves.

this approach is the most suitable is that transforming images implies integer round-off operations (due to the pixel-nature of images) – as opposed to transforming point coordinates.

Appendix D. Details of the 2D DDD computations

D.1. The 2D DDD simulation model

To numerically study the depinning phenomenon of dislocation lines in a heterogeneous stress field, a 2D grid model was employed that is based on the one used in [14]. The model mimics the motion of a single dislocation line in its glide plane due to an externally applied stress and captures the elastic interactions between different parts of a moving dislocation line as well as the effects of the random local lattice distortions.

The domain consists of a rectangular grid of size $L_x \times L_y$ (with periodic boundary conditions (PBCs) in horizontal x direction and a cell size equal to the lattice constant) that represents the slip plane of a gliding dislocation. Sites have binary values corresponding to plastic slip: sites that are already behind the dislocation line (slipped part) are assigned 1, and the others (unslipped part) are assigned the value of 0. The boundaries between different-valued sites represent dislocation segments. These segments are of either pure edge or pure screw character. That is, in the simulations the Burgers vector is chosen to be either parallel to the x or the y axis. The resolved shear stress σ acting on a segment at position $\boldsymbol{r}$ is the sum of four contributions:

$$\sigma(\boldsymbol{r}) = \sigma_{\text{ext}}(\boldsymbol{r}) + \sigma_{\text{self}}(\boldsymbol{r}) + \sigma_{\text{pin}}(\boldsymbol{r}) \,, \tag{D.2}$$

that is, the external stress σ_{ext}, the stress from the self-interaction of the dislocation σ_{self}, and the pinning field σ_{pin}. We chose the lattice constant to be equal to the size of the Burgers vector b, such that the line tension is included in the self-interaction term. The fluctuating lattice distortion of the HEA is captured by the pinning field σ_{pin}: an uncorrelated shear stress value is assigned to every cell drawn from a centered Gaussian distribution with standard deviation Σ_{pin}. The self-stress at the ith segment is the sum of the contributions of all other segments (and their images in direction x which ensures the PBCs):

$$\sigma_{\text{self}}(\boldsymbol{r}_i) = \sum_j^{\{s\}} \sigma_{\text{s}}(\boldsymbol{r}_i - \boldsymbol{r}_j) + \sum_j^{\{e\}} \sigma_{\text{e}}(\boldsymbol{r}_i - \boldsymbol{r}_j) \,, \tag{D.3}$$

where $\sigma_{\text{s}}(\boldsymbol{r})$ and $\sigma_{\text{e}}(\boldsymbol{r})$ are summed over the set of the other screw $\{s\}$ and edge segments $\{e\}$. For the details of the computation of the segment interactions see Appendix D.2.

The evolution of the dislocation line is modeled using random dynamics. This means that at every time step a segment is chosen

Table D.2
Self stress in different scenarios. b, μ and ν are the length of the Burgers vector, the shear modulus and the Poisson's ratio, respectively. $\boldsymbol{b}$, is the Burgers vector and $\boldsymbol{x}$ and $\boldsymbol{y}$ are unit vector in direction x and y. $\boldsymbol{r}$ is the relative position vector measured from the source and x and y are the relative coordinates. $\overline{S} = \pm 1$ and its value depends on the orientation of both interacting segments.

Source	$b \parallel x$	$b \parallel y$
$\sigma_s(\boldsymbol{r})$ (screw)	$\overline{S}\mu b^2 y/\left(4\pi r^3\right)$	$\overline{S}\mu b^2 x/\left(4\pi r^3\right)$
$\sigma_e(\boldsymbol{r})$ (edge)	$\overline{S}\mu b^2 x/\left[4\pi(1-\nu)r^3\right]$	$\overline{S}\mu b^2 y/\left[4\pi(1-\nu)r^3\right]$

Table D.3
Simulation parameters in simulation units where distance is measured in units of b and stress is in units of μ.

Symbol	Definition	Value
ν	Poisson ratio	0.35
B	stiffness constant	10^{-8}
$\Delta\sigma$	stress increment per timestep	10^{-10}
L_x	lattice width	400

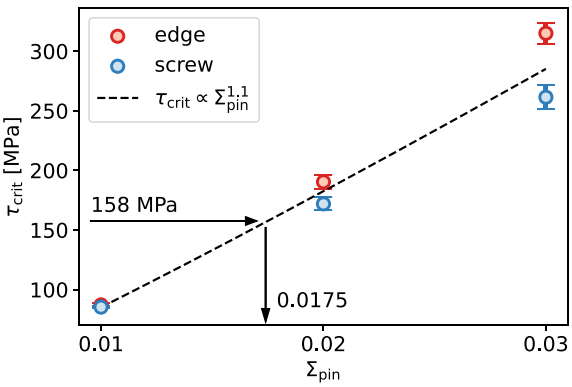

Fig. D.6. The scaling of critical stress σ_{yield} with pinning stress fluctuation Σ_{pin}. Arrows indicate to process of the interpolation of Σ_{pin}.

randomly and the local resolved shear stress is calculated for that segment from Eq. (D.2). Then the segment is moved in the direction of the gliding component of the Peach–Koehler force.

In order to study the stick–slip dynamics in the framework of this lattice model the following procedure was utilized. First, a configuration with a single straight dislocation line is created. Then, the above described random dynamics is employed. The external stress σ_{ext} is zero and then it is increased with a small constant increment $\Delta\sigma$ each timestep. Simultaneously, the external stress is changed with a value $-B\Delta A$ where $\Delta A = \pm b^2$ is the plastic slip increment and B is a constant characterizing the stiffness of the sample. Consequently, during a slip event with a positive plastic strain increment, the stress drops. As a result, after a transient, the system reaches a steady state with a zig-zag like stress-time curve characteristic of stick–slip dynamics. The statistical analysis of dynamics and the shape of the dislocation lines were executed on the steady state regime of the simulations. Parameters $\Delta\sigma$ and B were chosen in a manner that the stress changes very little each time step leading to a quasi-static simulation.

D.2. Interaction of dislocation segments

The interaction of dislocation segments is computed according to Table D.2 in the simulation. The sign $\overline{S}$ depends on both the source and the target segments in the following way. A sign of $S = \pm 1$ can be assigned to both interacting segments. It can be computed as

$$S = \boldsymbol{l}(\boldsymbol{x} + \boldsymbol{y}), \tag{D.4}$$

where $\boldsymbol{l}$ is the unit line vector and $\boldsymbol{x}$ and $\boldsymbol{y}$ are unit vector in direction x and y. Let us denote the signs of two interacting segments with S_1 and S_2. Then, if the character of the two segments is the same (e.g. they are both edge segments) the sign of the interaction is $\overline{S} = S_1 S_2$, otherwise $\overline{S} = -S_1 S_2$.

D.3. Parameters

The parameters used in the simulations presented in the main text are listed in Table D.3. To ensure a quasi-static simulation the parameters were chosen so $\Delta\sigma \ll B \ll \sigma_{yield}$ is satisfied where σ_{yield} is the critical stress characteristic to the steady state stick-and-slip dynamics.

D.4. Tuning the fluctuations of the pinning stress field

In order to model appropriately the specific material at hand, the standard deviation Σ_{pin} of the pinning stress should be chosen properly. To this end, the critical stress σ_{yield} of dislocation slip was tuned to match the experimental values. As the exact value of CRSS is not available for the temperature of 110 K maintained in our experiments, the CRSS was estimated with linear interpolation between 77 K and 293 K for which temperatures data is accessible in Ref. [54]. With interpolation, 158 MPa can be obtained. The conversion of simulation stresses to SI values can be done by multiplication with the shear modulus μ =84.65 GPa of the Cantor alloy. The critical stress of our model was measured for a few different values of Σ_{pin}. Then, the Σ_{pin} corresponding to the desired critical stress was obtained with interpolation (see Fig. D.6). Note, that our model exhibits a scaling of $\sigma_{yield} \propto \sigma_{pin}^{\gamma}$ with $\gamma \approx 1.1$ which is quite close to the theoretical expectation of $\gamma = 4/3$ for binary alloys [10]. The slight difference in the behavior of edge and screw dislocations can be explained by the energy difference of the two types of segments. Since screw segments are more energetically favorable, a screw dislocation is less willing to bow out (and create new edge segments in the process) resulting in lower critical stress.

Based on Fig. D.7 the tuning of Σ_{pin} is reasonable resulting in an average external stress in the stick–slip regime of (162 ± 5) MPa and (136 ± 6) MPa for edge and screw dislocations, respectively.

D.5. The robustness of the slip size distribution

While the simulated and the experimental data match very well in terms of the exponent of the slip size distribution for the chosen value of Σ_{pin}, the question emerges whether the exponent is universal. To prove that the extent of the fluctuation of internal pinning stresses (characterized by Σ_{pin}) were varied. Fig. D.8 demonstrated that the distribution (and the exponent τ in particular) is robust to the change of Σ_{pin}.

D.6. Discussion of the roughness exponent and its robustness

The power law avalanche statistics and the self-affine avalanche roughness revealed from the experimental data exhibit robust scaling exponent characteristics of the stick–slip motion of the dislocation line. Interestingly, these exponents hint at a so far not understood behavior since the roughness exponent ζ_{av} is rather different from those predicted by previous dislocation-based models of depinning. In particular, the quenched Edwards- Wilkinson (qEW) model (that assumes that dislocation line is equivalent to an elastic string without any long-range interactions) predicts $\zeta = 1.25$ [55], whereas using more precise discrete dislocation dynamics one obtains $\zeta \approx 1.0$ [14,56–58]. However, these models investigated the roughness of the whole dislocation line instead of the slipped areas during events, that is, the roughness exponent is defined as $\langle |y(x+d) - y(x)| \rangle_x \propto d^{\zeta}$, where $\langle \cdot \rangle_x$ denotes averaging over x. The two roughness exponents ζ and ζ_{av} are usually assumed to be equivalent, however, exceptions have already been found [59]. The avalanche size distributions have not yet been

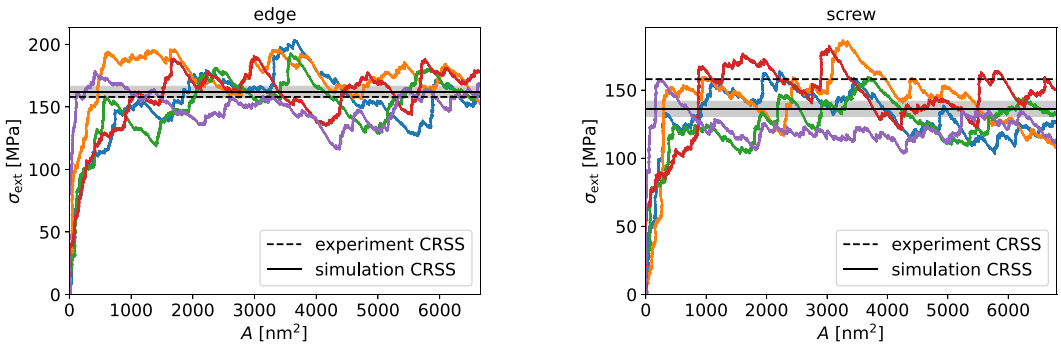

Fig. D.7. The simulated stress-slipped area curves for edge and screw dislocations at $\Sigma_{pin} = 0.0175$. The dashed line corresponds to the CRSS obtained with interpolation of prior experimental results. The solid line indicates the average external stress in the stick–slip regime with the transparent stripe showing its uncertainty computed with the jackknife method.

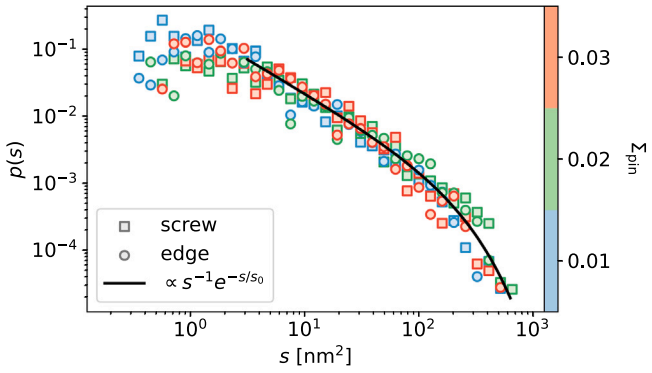

Fig. D.8. The slip size s distribution for different values of Σ_{pin} and different dislocation characters.

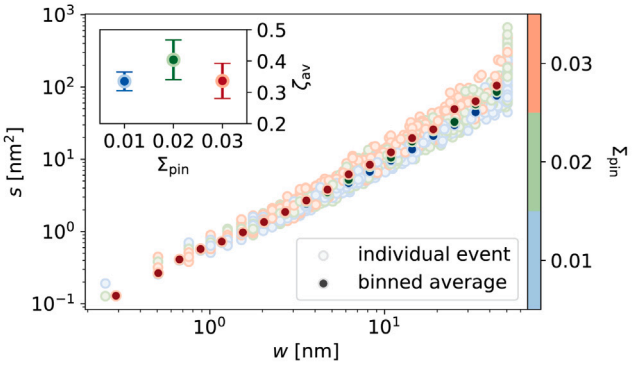

Fig. D.9. The scaling of slip size s with the slip width w (edge and screw dislocations are both included).

determined for single dislocation dynamics, but we note that the qEW model predicts $\tau = 1.11$ [60] in accordance with the scaling law

$$\tau = 2 - 2/(d + \zeta) \tag{D.5}$$

derived for depinning of 1D elastic lines ($d = 1$) with short-range self-interaction [61].

In order to fill the gap, a 2D DDD model has been developed based on [14] to provide a physics-based explanation of the experimental findings (see Methods and D for general descriptions of the model). To model the experimental conditions and the elastic stiffness of the loading cell, the external loading is performed through a spring which leads to a stress drop during every plastic avalanche and a constantly increasing stress between these events. Our results clearly show that there is a $s \propto w^{1+\zeta_{av}}$ relationship between the slip sizes s and slip widths w with $\zeta_{av} \simeq 0.35$. The exponent seems to be robust to the change of Σ_{pin} (see Fig. D.9).

ζ_{av} is unusually low in our simulations as compared to the roughness exponent ζ of 1.25 suggested by isotropic models of the depinning of elastic interfaces. We argue that this is due to dislocation segments interacting via highly anisotropic interaction. The quite low value of ζ_{av} can be also understood by studying the evolution of slip events. Our simulation data (for $\Sigma_{pin} = 0.0175$) shows that the total width w of an event scales with the slipped area A as $w \propto A^{\alpha_w}$ with $\alpha_w \approx 0.8$ and the height h of the event at its thickest part scales as $h \propto A^{\alpha_h}$ with $\alpha_h = 0.25 \sim 0.3$ see Fig. D.10. That is, in a typical event height of the affected area approaches its maximum value quickly and then only increases incrementally while the area growth is achieved predominantly by the widthening of the slipped surface. Consequently, the events are flat and one can obtain a low value for exponent ζ_{av}. We also note that the slight dependence of exponents α_w and α_h on the dislocation character is because events in screw dislocations are even flatter due to energetic reasons.

In the case of elastic interfaces with an isotropic force field, the exponent ζ characterizes the roughness of the interface (in this case, the dislocation line). Now the exponent extracted from dislocation line shapes is denoted ζ. One way to obtain this exponent is by analyzing the power spectrum of dislocation lines. Namely, if the power spectrum P (at low wave numbers k) obey

$$P(k) \propto k^{-\gamma}, \tag{D.6}$$

then

$$\zeta = \frac{\gamma - 1}{2}. \tag{D.7}$$

Our results yield an exponent of $\zeta \approx 0.85$ (see Fig. D.11). This is consistent with other works that have shown that for a relaxed line $\zeta = 0.5$ and as the system reaches the steady stick–slip regime ζ converges to 1 [57].

D.7. Supplementary movie of the 2D-DDD simulation

The supplementary movie of the 2D discrete dislocation dynamic simulation (`supplementary movie #5`) illustrates the propagation of a dislocation line along the y-direction on the left panel and the corresponding slipped surface-stress curve on the right panel. The active dislocation line is colored in gray while the passed dislocation line is colored with purple-to-greenish color with 50 % of the transparency to present the evolution of the dislocation.

Appendix E. Supplementary data

Supplementary material related to this article can be found online at https://doi.org/10.1016/j.actamat.2024.120455.

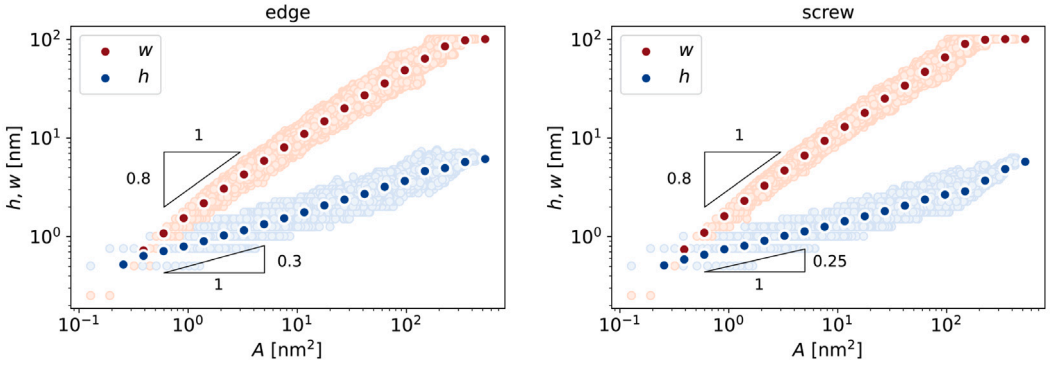

Fig. D.10. The evolution of the width w and height h of events in edge and screw dislocations as the slipped area A grows.

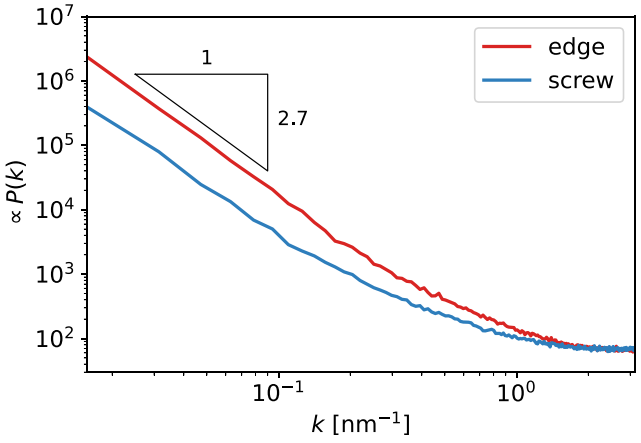

Fig. D.11. The power spectrum of dislocation lines in the stick–slip regime in systems with $\Sigma_{pin} = 0.0175$.

Data availability

Data is available in the form of supplementary movies, annotated training images and predictions from deep learning, as well as all shown postprocessed data. The data is provided as supplementary data and through https://zenodo.org/doi/10.5281/zenodo.10800695.

References

[1] B. Cantor, I. Chang, P. Knight, A. Vincent, Microstructural development in equiatomic multicomponent alloys, Mater. Sci. Eng. A 375 (2004) 213–218.

[2] J.-W. Yeh, S.-K. Chen, S.-J. Lin, J.-Y. Gan, T.-S. Chin, T.-T. Shun, C.-H. Tsau, S.-Y. Chang, Nanostructured high-entropy alloys with multiple principal elements: novel alloy design concepts and outcomes, Adv. Eng. Mater. 6 (5) (2004) 299–303.

[3] R. Zhang, S. Zhao, J. Ding, Y. Chong, T. Jia, C. Ophus, M. Asta, R.O. Ritchie, A.M. Minor, Short-range order and its impact on the CrCoNi medium-entropy alloy, Nature 581 (7808) (2020) 283–287, http://dx.doi.org/10.1038/s41586-020-2275-z.

[4] M.-H. Tsai, J.-W. Yeh, High-entropy alloys: a critical review, Mater. Res. Lett. 2 (3) (2014) 107–123.

[5] D. Miracle, High entropy alloys as a bold step forward in alloy development, Nature Commun. 10 (1) (2019) 1805.

[6] E. Ma, X. Wu, Tailoring heterogeneities in high-entropy alloys to promote strength–ductility synergy, Nature Commun. 10 (1) (2019) 5623.

[7] E.P. George, W. Curtin, C.C. Tasan, High entropy alloys: A focused review of mechanical properties and deformation mechanisms, Acta Mater. 188 (2020) 435–474.

[8] R. Feng, C. Zhang, M.C. Gao, Z. Pei, F. Zhang, Y. Chen, D. Ma, K. An, J.D. Poplawsky, L. Ouyang, et al., High-throughput design of high-performance lightweight high-entropy alloys, Nature Commun. 12 (1) (2021) 4329.

[9] D. Utt, S. Lee, Y. Xing, H. Jeong, A. Stukowski, S.H. Oh, G. Dehm, K. Albe, The origin of jerky dislocation motion in high-entropy alloys, Nature Commun. 13 (1) (2022) 4777.

[10] P.-A. Geslin, D. Rodney, Microelasticity model of random alloys. Part I: mean square displacements and stresses, J. Mech. Phys. Solids 153 (2021) 104479.

[11] P.-A. Geslin, A. Rida, D. Rodney, Microelasticity model of random alloys. part ii: displacement and stress correlations, J. Mech. Phys. Solids 153 (2021) 104480.

[12] G.P.M. Leyson, W.A. Curtin, L.G. Hector Jr., C.F. Woodward, Quantitative prediction of solute strengthening in aluminium alloys, Nature Mater. 9 (9) (2010) 750–755.

[13] C. Varvenne, A. Luque, W.A. Curtin, Theory of strengthening in fcc high entropy alloys, Acta Mater. 118 (2016) 164–176.

[14] S. Zapperi, M. Zaiser, Depinning of a dislocation: the influence of long-range interactions, Mater. Sci. Eng. A 309 (2001) 348–351.

[15] M. Kardar, Nonequilibrium dynamics of interfaces and lines, Phys. Rep. 301 (1–3) (1998) 85–112.

[16] D.S. Fisher, Collective transport in random media: from superconductors to earthquakes, Phys. Rep. 301 (1–3) (1998) 113–150.

[17] G. Blatter, M.V. Feigel'man, V.B. Geshkenbein, A.I. Larkin, V.M. Vinokur, Vortices in high-temperature superconductors, Rev. Modern Phys. 66 (4) (1994) 1125.

[18] M.D. Uchic, P.A. Shade, D.M. Dimiduk, Plasticity of micrometer-scale single crystals in compression, Annu. Rev. Mater. Res. 39 (2009) 361–386.

[19] J.R. Greer, J.T.M. De Hosson, Plasticity in small-sized metallic systems: Intrinsic versus extrinsic size effect, Prog. Mater. Sci. 56 (6) (2011) 654–724.

[20] W.C. Oliver, G.M. Pharr, An improved technique for determining hardness and elastic modulus using load and displacement sensing indentation experiments, J. Mater. Res. 7 (6) (1992) 1564–1583.

[21] X. Ma, W. Higgins, Z. Liang, D. Zhao, G.M. Pharr, K.Y. Xie, Exploring the origins of the indentation size effect at submicron scales, Proc. Natl. Acad. Sci. 118 (30) (2021).

[22] R. Schwaiger, B. Moser, M. Dao, N. Chollacoop, S. Suresh, Some critical experiments on the strain-rate sensitivity of nanocrystalline nickel, Acta Mater. 51 (17) (2003) 5159–5172.

[23] J. Weiss, D. Marsan, Three-dimensional mapping of dislocation avalanches: clustering and space/time coupling, Science 299 (5603) (2003) 89–92.

[24] P.D. Ispánovity, D. Ugi, G. Péterffy, M. Knapek, S. Kalácska, D. Tüzes, Z. Dankházi, K. Máthis, F. Chmelík, I. Groma, Dislocation avalanches are like earthquakes on the micron scale, Nature Commun. 13 (1) (2022) 1–10.

[25] W.D. Nix, H. Gao, Indentation size effects in crystalline materials: a law for strain gradient plasticity, J. Mech. Phys. Solids 46 (3) (1998) 411–425.

[26] N. Fleck, J. Hutchinson, A reformulation of strain gradient plasticity, J. Mech. Phys. Solids 49 (10) (2001) 2245–2271.

[27] M.-C. Miguel, A. Vespignani, S. Zapperi, J. Weiss, J.-R. Grasso, Intermittent dislocation flow in viscoplastic deformation, Nature 410 (6829) (2001) 667–671.

[28] D.M. Dimiduk, C. Woodward, R. LeSar, M.D. Uchic, Scale-free intermittent flow in crystal plasticity, Science 312 (5777) (2006) 1188–1190.

[29] F.F. Csikor, C. Motz, D. Weygand, M. Zaiser, S. Zapperi, Dislocation avalanches, strain bursts, and the problem of plastic forming at the micrometer scale, Science 318 (5848) (2007) 251–254.

[30] J. Weiss, W.B. Rhouma, T. Richeton, S. Dechanel, F. Louchet, L. Truskinovsky, From mild to wild fluctuations in crystal plasticity, Phys. Rev. Lett. 114 (10) (2015) 105504.

[31] P. Zhang, O.U. Salman, J.-Y. Zhang, G. Liu, J. Weiss, L. Truskinovsky, J. Sun, Taming intermittent plasticity at small scales, Acta Mater. 128 (2017) 351–364.

[32] P.D. Ispánovity, L. Laurson, M. Zaiser, I. Groma, S. Zapperi, M.J. Alava, Avalanches in 2D dislocation systems: Plastic yielding is not depinning, Phys. Rev. Lett. 112 (23) (2014) 235501.

[33] S.H. Oh, M. Legros, D. Kiener, G. Dehm, In situ observation of dislocation nucleation and escape in a submicrometre aluminium single crystal, Nature Mater. 8 (2) (2009) 95–100.

[34] M. Chen, E. Ma, K.J. Hemker, H. Sheng, Y. Wang, X. Cheng, Deformation twinning in nanocrystalline aluminum, Science 300 (5623) (2003) 1275–1277.
[35] S. Lee, M.J. Duarte, M. Feuerbacher, R. Soler, C. Kirchlechner, C.H. Liebscher, S.H. Oh, G. Dehm, Dislocation plasticity in FeCoCrMnNi high-entropy alloy: quantitative insights from in situ transmission electron microscopy deformation, Mater. Res. Lett. 8 (6) (2020) 216–224.
[36] D. Oliveros, A. Fraczkiewicz, A. Dlouhy, C. Zhang, H. Song, S. Sandfeld, M. Legros, Orientation-related twinning and dislocation glide in a Cantor High Entropy Alloy at room and cryogenic temperature studied by in situ TEM straining, Mater. Chem. Phys. 272 (2021) 124955.
[37] C. Zhang, H. Song, D. Oliveros, A. Fraczkiewicz, M. Legros, S. Sandfeld, Data-mining of in-situ TEM experiments: On the dynamics of dislocations in CoCrFeMnNi alloys, Acta Mater. 241 (2022) 118394.
[38] K. Govind, D. Oliveros, A. Dlouhy, M. Legros, S. Sandfeld, Deep learning of crystalline defects from TEM images: A solution for the problem of “never enough training data”, Mach. Learn.: Sci. Technol. (2023).
[39] K. Ruzaeva, K. Govind, M. Legros, S. Sandfeld, Instance segmentation of dislocations in TEM images, in: 2023 IEEE 23rd International Conference on Nanotechnology, NANO, IEEE, 2023, pp. 1–6, http://dx.doi.org/10.1109/NANO58406.2023.10231169.
[40] G. Po, Mechanics of defects evolution library (MoDELib), 2023, URL https://github.com/giacomo-po/MoDELib.
[41] Y. Cui, G. Po, N. Ghoniem, Controlling strain bursts and avalanches at the nano-to micrometer scale, Phys. Rev. Lett. 117 (15) (2016) 155502.
[42] H. Song, D. Dimiduk, S. Papanikolaou, Universality class of nanocrystal plasticity: localization and self-organization in discrete dislocation dynamics, Phys. Rev. Lett. 122 (17) (2019) 178001.
[43] Y. Sato, S. Shinzato, T. Ohmura, T. Hatano, S. Ogata, Unique universal scaling in nanoindentation pop-ins, Nature Commun. 11 (1) (2020) 1–9.
[44] J. Alcalá, J. Očenášek, J. Varillas, J. A El-Awady, J.M. Wheeler, J. Michler, Statistics of dislocation avalanches in FCC and BCC metals: dislocation mechanisms and mean swept distances across microsample sizes and temperatures, Sci. Rep. 10 (1) (2020) 1–14.
[45] M. Legros, M. Cabié, D.S. Gianola, In situ deformation of thin films on substrates, Microsc. Res. Techniq. 72 (3) (2009) 270–283, http://dx.doi.org/10.1002/jemt.20680, arXiv:https://analyticalsciencejournals.onlinelibrary.wiley.com/doi/pdf/10.1002/jemt.20680 URL https://analyticalsciencejournals.onlinelibrary.wiley.com/doi/abs/10.1002/jemt.20680.
[46] E. Ma, Unusual dislocation behavior in high-entropy alloys, Scr. Mater. 181 (2020) 127–133.
[47] A. Krizhevsky, I. Sutskever, G.E. Hinton, Imagenet classification with deep convolutional neural networks, Adv. Neural Inf. Process. Syst. 25 (2012).
[48] K. He, G. Gkioxari, P. Dollár, R. Girshick, Mask r-cnn, in: Proceedings of the IEEE International Conference on Computer Vision, 2017, pp. 2961–2969.
[49] O. Russakovsky, J. Deng, H. Su, J. Krause, S. Satheesh, S. Ma, Z. Huang, A. Karpathy, A. Khosla, M. Bernstein, et al., Imagenet large scale visual recognition challenge, Int. J. Comput. Vis. 115 (2015) 211–252.
[50] K. Govind, D. Oliveros, A. Dlouhy, M. Legros, S. Sandfeld, Deep learning of crystalline defects from TEM images: A solution for the problem of “never enough training data”, Mach. Learn.: Sci. Technol. (2024) http://dx.doi.org/10.1088/2632-2153/ad1a4e, URL https://iopscience.iop.org/article/10.1088/2632-2153/ad1a4e.
[51] G. Bradski, The OpenCV Library, Dr. Dobb’s J. Softw. Tools (2000).
[52] D.G. Lowe, Object recognition from local scale-invariant features, in: Proceedings of the Seventh IEEE International Conference on Computer Vision, Vol. 2, Ieee, 1999, pp. 1150–1157.
[53] B.D. Lucas, T. Kanade, An iterative image registration technique with an application to stereo vision, in: IJCAI’81: 7th International Joint Conference on Artificial Intelligence, Vol. 2, 1981, pp. 674–679.
[54] L. Patriarca, A. Ojha, H. Sehitoglu, Y. Chumlyakov, Slip nucleation in single crystal FeNiCoCrMn high entropy alloy, Scr. Mater. 112 (2016) 54–57.
[55] D. Rodney, P.-A. Geslin, S. Patinet, V. Démery, A. Rosso, Does the Larkin length exist? Modelling Simul. Mater. Sci. Eng. (2023).
[56] B. Bakó, D. Weygand, M. Samaras, W. Hoffelner, M. Zaiser, Dislocation depinning transition in a dispersion-strengthened steel, Phys. Rev. B 78 (14) (2008) 144104.
[57] J.-H. Zhai, M. Zaiser, Properties of dislocation lines in crystals with strong atomic-scale disorder, Mater. Sci. Eng. A 740 (2019) 285–294.
[58] G. Péterffy, P.D. Ispánovity, M.E. Foster, X. Zhou, R.B. Sills, Length scales and scale-free dynamics of dislocations in dense solid solutions, Mater. Theory 4 (1) (2020) 1–25.
[59] L. Laurson, S. Santucci, S. Zapperi, Avalanches and clusters in planar crack front propagation, Phys. Rev. E 81 (4) (2010) 046116.
[60] A. Rosso, P. Le Doussal, K.J. Wiese, Avalanche-size distribution at the depinning transition: A numerical test of the theory, Phys. Rev. B 80 (14) (2009) 144204.
[61] O. Narayan, D.S. Fisher, Threshold critical dynamics of driven interfaces in random media, Phys. Rev. B 48 (10) (1993) 7030.